



Molten salt synthesis of tetragonal carbon nitride hollow tubes and their application for removal of pollutants from wastewater

Liang Tian^{a,1}, Junyi Li^{a,1}, Feng Liang^{a,*}, Junkai Wang^a, Saisai Li^a, Haijun Zhang^{a,*}, Shaowei Zhang^b

^a The State Key Laboratory of Refractories and Metallurgy, Wuhan University of Science and Technology, Wuhan 430081, China

^b College of Engineering, Mathematics and Physical Sciences, University of Exeter, Exeter Ex4 4QF, UK

ARTICLE INFO

Keywords:

Carbon nitride
Molten salt
Tetragonal hollow tube
Photocatalytic degradation
Adsorption performance

ABSTRACT

Carbon nitride has attracted extensive attention because of its promising properties and great application potential in photocatalysis, electrocatalysis, bioimaging and biomedicine. In this work, carbon nitride with a novel morphology, i.e., tetragonal carbon nitride hollow tube (TCNT), was in-situ synthesized by a molten salt method at 450 °C using melamine as the starting precursor. As-prepared TCNTs were 2–20 μm long and 50–2000 nm wide and possessed higher content of impurity nitrogen and larger specific surface area than conventional bulk g-C₃N₄ (B-CN). A possible salt-assisted self-assembly mechanism is believed to have dominated the formation of TCNTs. As-prepared TCNTs exhibited superior photocatalytic activities and adsorption performance for methylene blue and phenol degradation to B-CN, suggesting that they could be potentially used as a promising photocatalyst and adsorbent.

1. Introduction

Owing to its unique electronic band structure and high thermal and chemical stability, carbon nitride is widely used in photoelectrochemistry, catalysis for important reactions, photocatalysis for hydrogen generation from water, CO₂ reduction, degradation of organic pollutants, and electrochemical sensors [1–7]. Generally, bulk g-C₃N₄ (B-CN) can be readily fabricated by direct pyrolysis of nitrogen-rich precursors such as cyanamide, dicyandiamide, melamine, urea, thiourea, and ammonium thiocyanate [8–13]. Nevertheless, the B-CN resultant from this route usually has relatively poor performance due to its low specific surface area and rapid recombination rate of photoexcited charge carriers.

As well known, low dimensional materials possessing high specific surface area and exceptionally high anisotropy generally exhibit unique electronic structures and excellent physicochemical properties. Hence, many low dimensional carbon nitride materials, e.g., quantum dots [14], nanorods [15,16], nanotubes [17] and nanosheets [18–20], have been fabricated to increase their specific surface area and optimize their performances. The template, molecular self-assembly and chemical exfoliation methods are the most commonly used ways for preparing low dimensional carbon nitride. Nevertheless, all these methods suffer from several disadvantages such as complex processes, high production

cost and low product yield.

Molten salt synthesis has been proved to be a green process to prepare a wide range of nanomaterials with controllable nanostructure [21–24]. It has been used recently to prepare 2D crystalline carbon nitride [25–29], such 2D carbon nitride material is composed of imide-linked triazine units (Poly (triazine imide), C₃N₃), rather than tri-triazine units (heptazine, C₆N₇) in B-CN, resulting in much improved visible-light photocatalytic activities.

In the present work, a novel form of tetragonal carbon nitride hollow tube (TCNT) was prepared for the first time via a facile and controllable molten salt route. As-prepared TCNTs exhibited superior photocatalytic activities and adsorption performance in the cases of degradation of methylene blue and phenol to B-CN, owing to their unique one-dimensional hollow structures. This, along with other results, will be presented and discussed in this paper, and a plausible salt-assisted self-assembly mechanism for the formation of TCNTs will be also proposed.

2. Experimental procedure

2.1. Preparation of samples

Two series of samples were prepared to clarify the effect of reaction

* Corresponding authors.

E-mail addresses: liangfengref@wust.edu.cn (F. Liang), zhanghaijun@wust.edu.cn (H. Zhang).

¹ Authors contributed equally to this work.

temperature and holding time on the formation of TCNTs, the first ones were synthesized at 400 °C, 450 °C, 500 °C, 550 °C and 600 °C for 5 h (denoted as CN400, CN450, CN500, CN550 and CN600, respectively), and the second ones at 450 °C for 1 h, 3 h and 5 h (denoted as CN1 h, CN3 h and CN5 h, respectively) in a LiCl (or LiBr)-KCl medium. In a typical process, for the case of CN450 (also denoted as TCNTs), 1 g melamine was milled together with 20 g of eutectic mixture of LiCl (or LiBr) and KCl (in the weight ratio of 45:55, with the eutectic point of 352 °C for LiCl-KCl; and in the weight ratio of 75:25, with the eutectic point of 309 °C for LiBr-KCl). The mixed powder was placed in an alumina crucible with a lid and heated at 4 °C/min to 450 °C and held for 5 h in air. After furnace-cooling to room temperature, the reacted mass was washed repeatedly with distilled water to remove the residual salt. The resultant product powder was oven-dried overnight at 80 °C prior to further characterization and testing.

In addition, for comparison, B-CN was prepared by using the conventional method reported previously. In this case, typically 10 g melamine was placed in an alumina crucible with a lid, and heated at 4 °C/min to 550 °C and kept for 5 h. The resultant yellow material was milled to fine powders using a mortar and pestle.

2.2. Sample characterization

Phases in samples were identified by using an X-ray diffractometer (XRD, X'Pert Pro, Philips, Netherlands) with Cu-K α radiation ($\lambda = 1.5406$ Å) operated at 40 kV and 40 mA, at a scanning rate of 2°(2 θ)/min and a step size of 0.02° (2 θ). Fourier transform infrared (FTIR) spectra of samples (embedded in KBr pellet) were recorded within the frequency range of 4000–400 cm⁻¹ and with a resolution of 4 cm⁻¹ using a FTIR spectrometer (VERTEX 70, Germany). X-ray photo electron spectroscopy (XPS) examination was carried out on a VG Multilab 2000 instrument (Thermo Electron Co., USA) using 300 W Al K α as the excitation source. Samples in this case were subjected to high vacuum before being introduced into the analysis chamber. The binding energies from XPS were referenced to the C1s binding energy (284.6 eV) of “adventitious” carbon contamination. Morphologies of product phases were examined using a field emission scanning electron microscope (FESEM, Novo 400, FEI Co., USA) and a transmission electron microscope (TEM, 2000F, Jeol Ltd., Japan) (TEM samples were loaded on a copper microgrid that was covered with a thin amorphous carbon films) equipped with an energy dispersive spectrometer (EDS, Penta FET X-3 Si (Li)). Nitrogen adsorption-desorption was examined at 77 K on an automatic surface area and pore size analyzer (Autosorb-1, USA). In this case, all the samples were pre-degassed at 393 K for 3 h, and the Brunauer-Emmett-Teller (BET) surface area was calculated according to the adsorption isotherm. UV–vis absorption spectra were recorded using a UV–vis spectrophotometer (Shimadzu UV-3600, Japan). High performance liquid chromatography (Agilent 1100series, USA) was used to measure the phenol concentration.

2.3. Measurement of photocatalytic activity

Photocatalytic activities of as-prepared samples were illustrated by photodegradation of methylene blue and phenol under visible light irradiation from a 300 W Xe lamp with a 420 nm cutoff filter. For a typical photocatalytic test, a total of 50 mg and 100 mg of as-prepared samples were respectively dispersed in aqueous solution of methylene blue (250 mL, 3.2 mg/L) and phenol (100 mL, 10 mg/L). The suspensions were magnetically stirred in darkness for 1 h to ensure the adsorption/desorption equilibrium between methylene blue and the photocatalyst and then placed in a magnetic stirrer at a rate of 150 rpm at 288 K under visible light irradiation, during which 3 mL suspension was periodically taken from the reactor at given time intervals and centrifuged/filtered to measure the dye concentration using UV–vis spectrophotometer and high performance liquid chromatography.

2.4. Evaluation of adsorption performance

Adsorption properties of samples were investigated using methylene blue as an adsorbate. Typically, 30 mg of as-prepared sample powders were added into a beaker containing 30 mL aqueous solution of methylene blue with concentration ranging from 0 to 15 mg/L. The suspension was then subject to 1 h magnetic stirring at 150 rpm at 288 K. After centrifugation, the dye solution concentration was measured using the UV–vis spectrophotometer.

The adsorption kinetics of as-prepared B-CN and TCNTs were carried out. 60 mg of as-prepared sample powders were added to a methylene blue aqueous solution (60 mL, 3 mg/L) in a beaker. The suspension was then subject to magnetic stirring at 150 rpm at 288 K, during which 3 mL suspension was sampled at pre-determined time intervals and centrifuged to measure the dye concentration using the UV–vis spectrophotometer.

The equilibrium adsorption amount was calculated according to the following equation:

$$q_e = \frac{(C_0 - C_e)V}{m} \quad (1)$$

where q_e (mg g⁻¹) is the equilibrium adsorption amount, C_0 (mg L⁻¹) the initial concentration of dye solution, C_e (mg L⁻¹) the equilibrium concentration of dye solution, V (L) the volume of dye solution, and m (g) the mass of the absorbent.

3. Results and discussion

3.1. Structure and morphology of samples

XRD patterns of as-prepared TCNTs and B-CN are shown in Fig. 1a. In the case of B-CN, two diffraction peaks appeared respectively at 27.40° and 13.04° (2 θ). The former corresponded to characteristic interplanar stacking of aromatic rings (indexed as (002) peak), and the latter to the in-plane structural motif (indexed as (100)). In the case of TCNTs, however, a quite different XRD pattern (with the space group $P6_3cm$, $a = b = 8.434$ Å, and $c = 6.722$ Å) was obtained (Fig. 1a). The strongest peak at 26.6°, which arose from stacking of conjugated aromatic units, can be indexed as (002). And the corresponding interplanar distance of 0.335 nm matched well with the d_{002} spacing (0.34 nm) in crystalline g-C₃N₄. Moreover, another characteristic peak at 11.9° indexed as (100), can be ascribed to the in-plane structure motif of nascent sheet of planar carbon nitride. The corresponding interplanar distance in this case (0.74 nm) also matched with the size of poly (triazine imide) [25,26]. These results suggested that as-prepared TCNTs were of high crystalline extent and high purity.

FTIR spectra were used to identify the chemical functional groups of as-prepared TCNTs and B-CN (Fig. 1b). The broad bands at 3000–3300 cm⁻¹ corresponded to N–H stretching and O–H interactions due to residual amino groups and absorbed H₂O. Several strong peaks between 1200–1650 cm⁻¹ were associated with stretching vibrations of CN heterocyclic units. Additionally, the sharp peak at 806 cm⁻¹ arose from characteristic bending vibration of triazine units. It is worth mentioning that tri-s-triazine unit has a rigid D_{3h} symmetry plane geometry and considerable conjugation heterocycle with a characteristic vibrational frequency at about 869.8 cm⁻¹, which could be used to distinguish it from s-triazine [30]. As seen from Fig. 1b, a characteristic frequency at about 869.8 cm⁻¹ was present in the FTIR spectra of B-CN, but absent from the spectra of TCNTs, which seemed to suggest that TCNTs were composed of s-triazine rather than tri-s-triazine.

XPS was carried out to further reveal the chemical composition and chemical state in B-CN and TCNTs. B-CN and TCNTs were both composed of mainly C, N and O (Fig. S1a and b, Table S1). The high-resolution XPS C 1s gave two peaks (Fig. S1c and d). The one at 287.7 eV corresponded to sp²-hybridized carbon bonded to nitrogen in aromatic

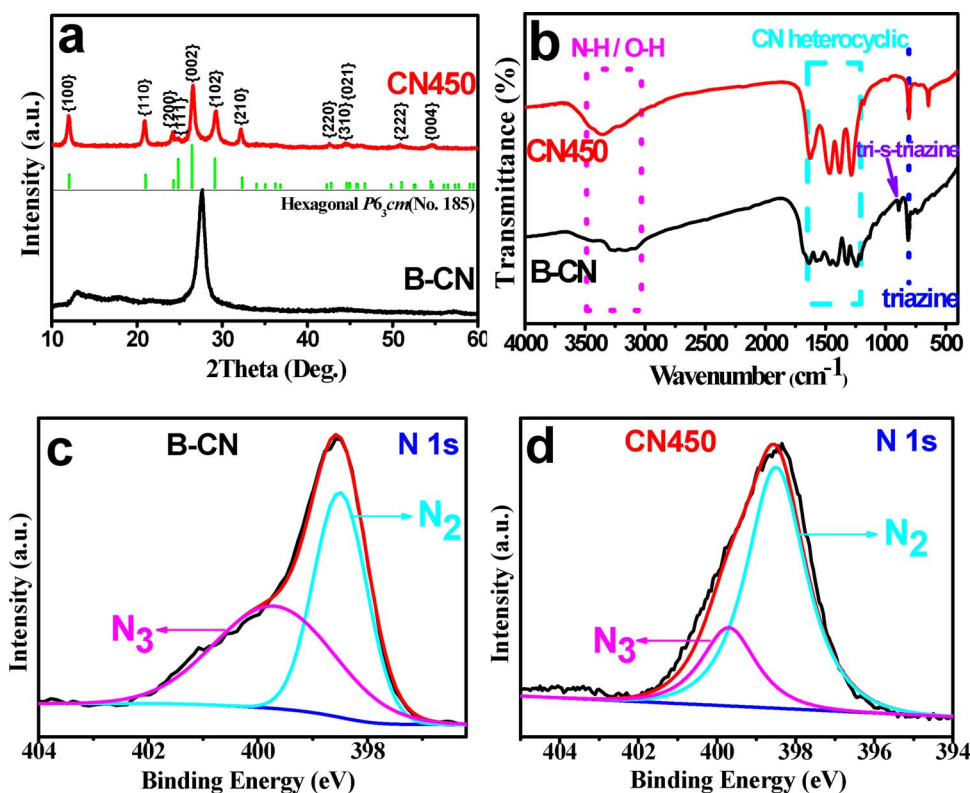


Fig. 1. XRD patterns (a) and FTIR spectra (b) of B-CN (black line) and TCNTs (red line), and high resolution N 1 s XPS spectra of B-CN (c) and TCNTs (d). (For interpretation of the references to colour in this figure legend, the reader is referred to the web version of this article.)

rings ($\text{N}=\text{C}=\text{N}$), and the other at 284.6 eV arose from sp^2 C–C bonding in the standard reference carbon. The high-resolution XPS O 1 s also gave two peaks (Fig. S1e and f), ascribed respectively to H_2O (532.1 eV) and O_2 (530.8 eV) [28]. Therefore, it can be reasonably considered that the oxygen element in XPS was derived from adsorbed water and air. As shown in Fig. 1c and d, two peaks also appeared after deconvolution of the N 1 s spectra. The primary peak at 398.5 eV was associated with sp^2 -hybridized N involved in triazine rings ($\text{C}=\text{N}=\text{C}$, N_2). The other peak at 399.7 eV was attributed to N_3 , corresponding to $\text{N}(\text{C}_3\text{N}_3)$ in the case of B-CN and bridging N atoms in $\text{NH}(\text{C}_3\text{N}_3)_2/\text{LiN}(\text{C}_3\text{N}_3)_2$ in the case of TCNT, respectively [28]. These chemical states of C and N elements verified the existence of s-triazine structure, i.e., the basic structural unit of g- C_3N_4 . Moreover, the peak area ratio of the N_2/N_3 was calculated to be 1/1 in the case of B-CN, which was much smaller than that (about 3.1/1) in the case of TCNT. On the other hand, the atom ratio of N/C in the case of TCNT (1.17/1, Table S1) was also higher than that (0.84/1, Table S1) in the case of B-CN. These results indicated that as-prepared TCNTs contained more impurity nitrogen [31], which further suggested that nitrogen was more easily captured in molten salt medium during the process of melamine polymerization.

Morphologies of B-CN and TCNTs were examined by SEM and TEM. As shown in Fig. 2a, B-CN particles and chunks with sizes up to several micrometres were formed. On the other hand, an obvious tetragonal tubular morphology was seen in the case of TCNTs (Fig. 2b). TCNTs were 2–20 μm long and 50–2000 nm wide. A TEM image (Fig. 2c) revealed more clearly the tetragonal hollow tubular structure of as-prepared TCNTs. The tube walls appeared to be rough, due to the formation of lots of small nanoparticles on them (Fig. 2d). The SAED pattern (insert of Fig. 2d) showed two diffraction rings corresponding to {220} and {400} planes of TCNTs, which was consistent with the XRD pattern in Fig. 1a. EDS elemental analysis (on the area indicated by the red square in Fig. 2d) verified that TCNTs comprised C and N elements (the excessive carbon might be from the carbon support films used) (Fig. 2e).

Nitrogen sorption isotherms of TCNTs and B-CN are given in Fig. 2f, showing that the BET surface area in the case of the former was

128 m^2/g , whereas it was only 7 m^2/g in the case of the latter. The considerably higher surface area of TCNTs is believed to arise from their hollow tubular morphology and relatively rough surface.

3.2. Formation mechanism of TCNTs

In order to clarify the effect of reaction temperature on the formation of TCNTs in molten salt, the samples were also prepared by at various temperatures, and examined by XRD (Fig. S2). At 400 $^\circ\text{C}$, polymeric melam was formed from melamine. Upon increasing the temperature to above 450 $^\circ\text{C}$, the XRD pattern of the fired sample became similar to that in Fig. 1a, indicating the formation of polymeric carbon nitride. Furthermore, diffraction intensity corresponding to the {100} plane of carbon nitride was initially strong at 450 $^\circ\text{C}$ but became weaker at a higher reaction temperature, indicating that TCNTs were formed at 450 $^\circ\text{C}$ but their crystal structures still changed with the reaction temperature. As shown in Fig. S3, the intensities of N–H, CN heterocyclic and triazine groups also decreased with the increase in temperature, which was consistent with the XRD results. Morphological changes of samples with reaction temperature are demonstrated in Fig. S4. At 400 $^\circ\text{C}$, the product phases were formed as irregular shaped chunks. On increasing the temperature to above 450 $^\circ\text{C}$, tetragonal tubular nano-structured carbon nitride was formed in the final sample. Its yield was the largest at 450 $^\circ\text{C}$ but also decreased with the reaction temperature. Upon increasing the temperature to 600 $^\circ\text{C}$, tetragonal tubular carbon nitride disappeared completely. These results were also consistent with those of XRD and FTIR (Figs. S2 and 3).

The effect of reaction time on the TCNT formation was also investigated. As shown in Fig. 3a, after 1 h reaction, nanoparticles with an average diameter of 100 nm were formed predominantly in the fired sample. After 3 h reaction, nanoplate phases started to form, and some of them showed the tendency to curl with right angle folds (Fig. 3b). Upon further increasing the reaction time to 5 h, large amounts of tetragonal tubular nanophases were formed, whereas the nanoplate phases almost completely disappeared (Fig. 3c).

Based on the above results, a plausible salt-assisted self-assembly

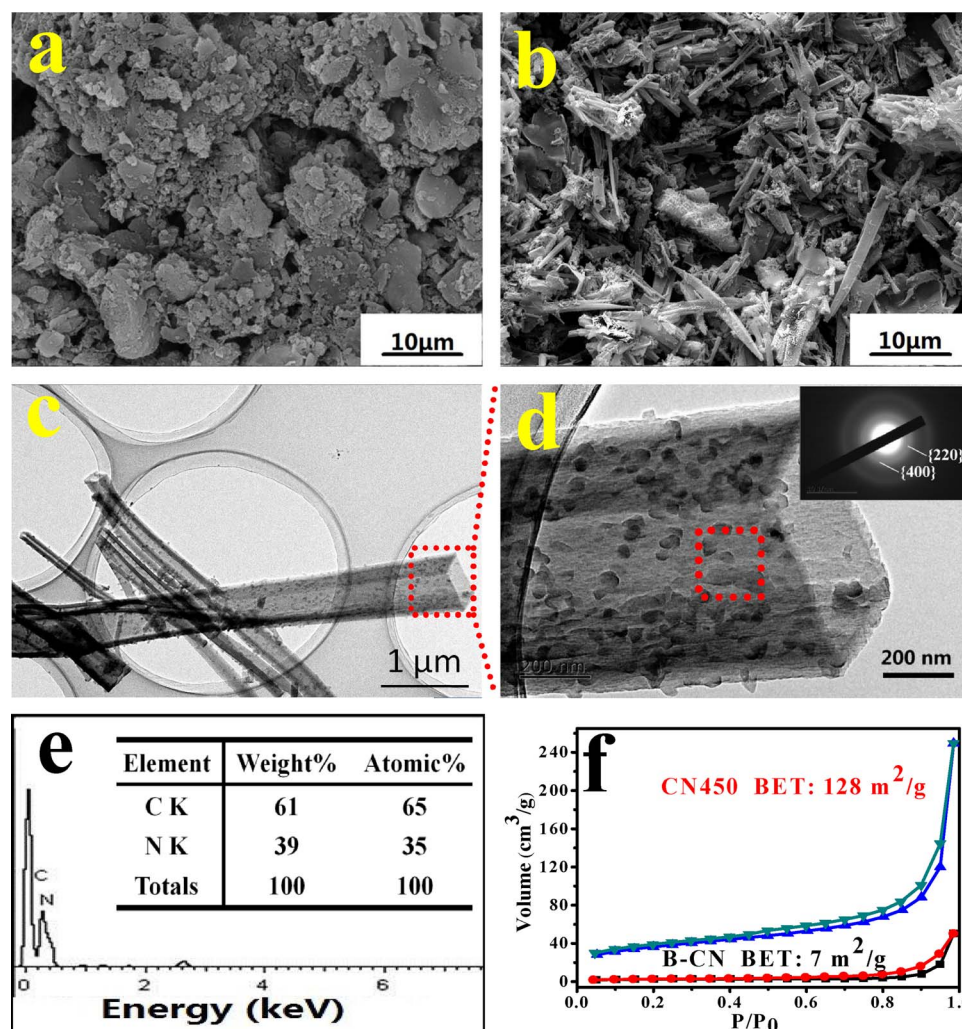


Fig. 2. SEM images of B-CN (a) and TCNTs (b), TEM image (c), high-resolution TEM image (d) and corresponding EDS (e) of TCNTs, and N_2 adsorption-desorption isotherms (f) of B-CN and TCNTs.

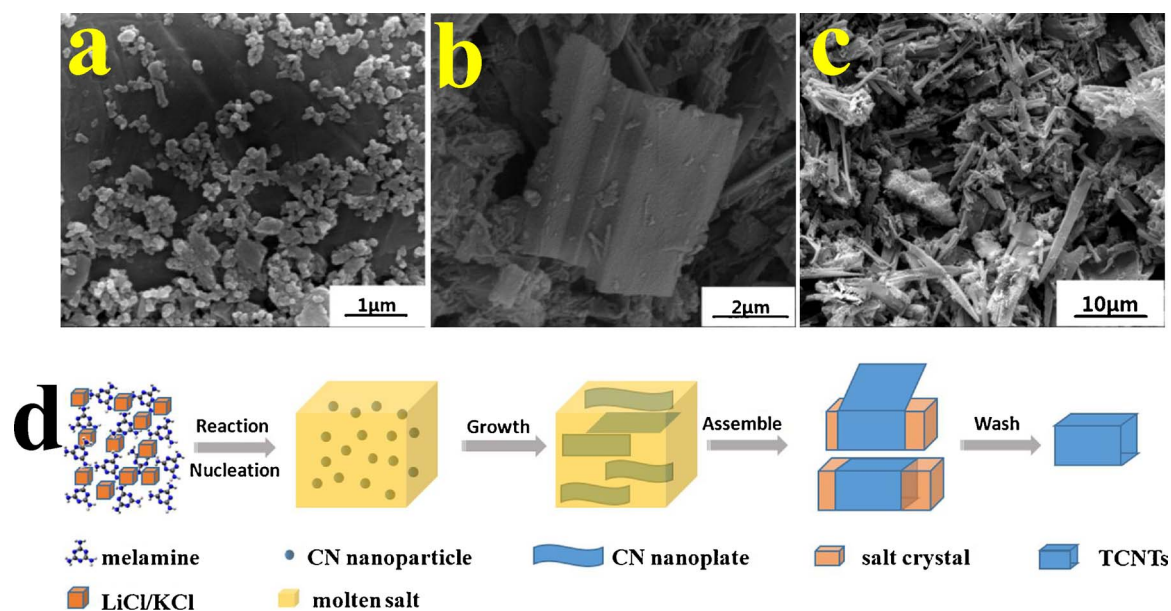


Fig. 3. SEM images of products resultant from firing at 450 $^{\circ}\text{C}$ for 1 h (a), 3 h (b) and 5 h (c), respectively, and schematic illustration of the formation process of TCNTs in the molten salt medium (d).

mechanism can be proposed for the TCNT formation and schematically illustrated in Fig. 3d: 1) In the initial stage of the molten salt process, as soon as the molten salt was oversaturated with thermally pyrolyzed and polycondensed melamine, carbon nitride would start to nucleate and grow, forming predominantly carbon nitride nanoparticles (Fig. 3a); 2) Similarly to layer-structured graphite, carbon nitride nanoparticles tended to merge and grow together, forming carbon nitride nanoplates/nanosheets under the actions of highly reactive lithium ions, potassium ions and chloride ions [32] in the molten salt medium (Fig. 3b); 3) On cooling, the recrystallized salt with a cubic structure (Fig. S5, K and Cl were detected by EDS in the recrystallized salt, but Li was not detectable because it was beyond the element detection range of Be4-U92.) acted as an in-situ template on which carbon nitride nanoplates formed earlier curled, forming the tubular nanostructured-carbon nitride (Fig. 3c). Such a behavior is believed to be driven by minimization of the overall surface free energy [33]; 4) Finally, TCNTs were obtained after water-leaching the salt template inside.

3.3. Photocatalytic activities of samples

As shown in Fig. S6, the UV–vis absorption intensity of TCNTs increased evidently and their band gap decreased from 2.76 (in the case of B-CN) to 2.28 eV. It is believed that the impurity nitrogen defects in TCNT led to some localized energy levels in the band gap, and then extended the light absorption. Similar phenomenon was commonly observed in doped TiO₂ and other semiconducting photocatalytic materials [34]. Hence, it is reasonable to expect that they would have better photocatalytic activities. Photocatalytic activities of as-prepared samples were evaluated by examining the photodegradation behavior of methylene blue under visible light ($\lambda > 420$ nm) irradiation (Fig. 4 and Fig. S7). The TCNTs prepared by polycondensation in the molten salt medium showed a rapid photodegradation rate than B-CN. Notably, in the case of using TCNTs molten salt synthesized at 450 °C, almost all of the dye was degraded after 1.5 h visible-light irradiation, whereas in the case of using B-CN, only 75% degraded. The photocatalytic degradation reaction kinetics in both cases can be quantified by the following pseudo-first-order kinetic equation:

$$\ln\left(\frac{C}{C_0}\right) = -kt \quad (2)$$

where k is the apparent kinetic rate constant, C_0 and C are respectively the initial concentration at $t = 0$ and instantaneous concentration of the methylene blue solution at irradiation time t .

The kinetic rate in the case of using TCNTs (k , 1.72 h^{−1}, Table S2) was about twice as high as that in the case of using B-CN (k , 0.83 h^{−1}, Table S2), suggesting superior photocatalytic activities of TCNTs.

Moreover, the k value (with correlation coefficients of $R^2 > 0.99$) of samples prepared at different reaction conditions followed the order of CN450 (1.72 h^{−1}) > CN500 (1.42 h^{−1}) > CN3 h (1.25 h^{−1}) > CN550 (1.02 h^{−1}) > CN1 h (0.99 h^{−1}) > CN600 (0.84 h^{−1}) > B-CN (0.83 h^{−1}) (Table S2). It was notable that there was no obvious relationship between the specific surface area of as-prepared samples and photocatalytic degradation rates, as shown in Fig. S8 and Table S2. This was because the reaction rate in the most cases of solid-liquid phase photocatalysis is essentially limited by charge separation rather than mass transfer [35,36]. The much high photocatalytic activities of TCNTs can be ascribed to the high contents of impurity nitrogen defects present in the TCNTs, which results in localizing energy levels in the band gap and a decrease of the band gap.

Phenol was also used as a model non-dye pollutant to examine the photocatalytic activities of as-prepared samples. As shown in Fig. S9, the kinetic rate in the case of using TCNTs (k , 0.0948 h^{−1}) was also much higher than that in the case of using B-CN (k , 0.0576 h^{−1}), revealing further superior photocatalytic activities of TCNTs.

3.4. Adsorption performance of samples

Adsorption capacities of as-prepared B-CN and TCNTs for methylene blue were also examined, and the adsorption isotherms were simulated using the following non-linear forms of Langmuir (Fig. S10a) and Freundlich models (Fig. S10b):

$$q_e = \frac{Q_0 b C_e}{1 + b C_e} \quad (3)$$

$$q_e = k_F C_e^{1/n} \quad (4)$$

where q_e (mg g^{−1}) is the equilibrium adsorption amount, Q_0 (mg g^{−1}) is the maximum adsorption amount, b (L mg^{−1}) is the constant term related to the energy of adsorption, C_e (mg L^{−1}) is the equilibrium concentration of dye solution. k_F and n are the Freundlich constants, k_F represents the adsorption capacity of the adsorbent and n indicates favorable extent of the adsorption process ($n = 2-10$, $1-2$, and < 1 indicates respectively good, moderate and poor adsorption[37]).

The calculated adsorption parameters and correlation coefficients (R^2) based on Eqs. (3) and (4) are given in Table S3. The R^2 values of Langmuir and Freundlich models in the cases of using B-CN (0.9867 for Langmuir, and 0.9653 for Freundlich) and TCNTs (0.9924 for Langmuir, and 0.8886 for Freundlich) suggested that the Langmuir model is more accurate. The n values range from 3.03 to 3.70, suggesting the good adsorption ability of as-prepared samples. Moreover, the adsorption capacity of TCNTs (Q_0 , 7.22 mg g^{−1}) was found to be four times higher than that of B-CN (Q_0 , 1.28 mg g^{−1}). In addition, the Q_0 value (with correlation coefficients of $R^2 > 0.99$) of samples prepared at

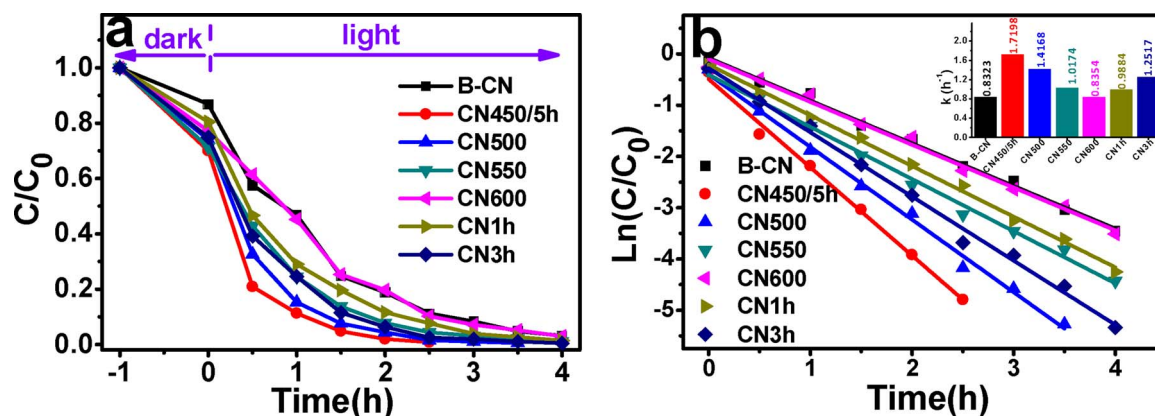


Fig. 4. Relative concentration (a) and Ln (relative concentration) (b) of the methylene blue solution as a function of time, under visible light irradiation ($\lambda > 420$ nm) over as-prepared samples.

Table 1
Adsorption kinetic parameters calculated based on Eqs. (3)–(5).

Sample	Freundlich			Langmuir			Pseudo-second-order		
	k_F	n	R^2	Q_0	b	R^2	q_e	k	R^2
B-CN	0.63	3.33	0.9653	1.28	0.86	0.9864	0.78	0.11	0.9997
TCNTs	4.22	3.70	0.8886	7.22	1.99	0.9924	2.28	1.42	0.9997

different reaction conditions followed the order of CN450 (7.22 mg g^{-1}) > CN550 (5.42 mg g^{-1}) > CN500 (5.00 mg g^{-1}) > CN3 h (4.18 mg g^{-1}) > CN600 (3.30 mg g^{-1}) > CN1 h (2.59 mg g^{-1}) > B-CN (1.28 mg g^{-1}) (Table S2), which showed a good correlation with specific surface area.

The kinetics of methylene blue removal was studied to further understand the adsorption behavior of as-prepared B-CN and TCNTs, and the results are shown in Fig. S11, and described by the following pseudo-second-order kinetic equation:

$$\frac{t}{q_t} = \frac{1}{kq_e^2} + \frac{t}{q_e} \quad (5)$$

where q_t (mg g^{-1}) is the adsorption amount at time t , and k ($\text{g mg}^{-1} \text{ min}^{-1}$) is the pseudo-second-order rate constant. The calculated kinetic parameters and correlation coefficients (R^2) based on Eq. (5) are listed in Table 1. As shown, the k value in the case of using TCNTs is almost thirteen times as large as that in the case of using B-CN, indicating evidently much rapider adsorption in the former.

4. Conclusions

TCNTs of 2–20 μm long and 50–2000 nm wide were successfully synthesized via a facile molten salt route. They exhibited much higher photocatalytic activities and better adsorption performance than B-CN owing to their higher content of impurity nitrogen, unique one-dimensional hollow structure and larger specific surface area. The formation of TCNTs was most likely governed by a salt-assisted self-assembly mechanism, opening a new avenue to controllable preparation of various one-dimensional hollow structured nanomaterials. TCNTs prepared in this work could be potentially used as an efficient, cost-effective and green catalyst for removal of pollutants from wastewater.

Acknowledgement

This work was financially supported by the National Natural Science Foundation of China, Grant No. 51502216, 51472184, 51472185; China Postdoctoral Science Foundation, Grant No. 2014M560631; Key Program of Natural Science Foundation of Hubei Province, Grant No. 2017CFA004; and Program for Innovative Teams of Outstanding Young and Middle-aged Researchers in the Higher Education Institutions of Hubei Province, Grant No. T201602.

Appendix A. Supplementary data

Supplementary data associated with this article can be found, in the online version, at <https://doi.org/10.1016/j.apcatb.2017.11.082>.

References

- [1] W.J. Ong, L.L. Tan, H.N. Yun, S.T. Yong, S.P. Chai, Graphitic carbon nitride ($\text{g-C}_3\text{N}_4$)-based photocatalysts for artificial photosynthesis and environmental remediation: are we a step closer to achieving sustainability? *Chem. Rev.* 116 (12) (2016) 7159–7329.
- [2] J. Jin, X. Fu, Q. Liu, J. Zhang, A highly active and stable electrocatalyst for the oxygen reduction reaction based on a graphene-supported $\text{g-C}_3\text{N}_4$ @cobalt oxide core-shell hybrid in alkaline solution, *J. Mater. Chem. A* 1 (1) (2013) 10538–10545.
- [3] S. Yang, X. Feng, X. Wang, K. Müllen, Graphene-based carbon nitride nanosheets as efficient metal-free electrocatalysts for oxygen reduction reactions, *Angew. Chem. Int. Ed.* 50 (23) (2011) 5339–5343.
- [4] J. Luo, G. Dong, Y. Zhu, Z. Yang, C. Wang, Switching of semiconducting behavior from n-type to p-type induced high photocatalytic NO removal activity in $\text{g-C}_3\text{N}_4$, *Appl. Catal. B* 214 (2017) 46–56.
- [5] Z. Sun, J.M.T.A. Fischer, Q. Li, J. Hu, Q. Tang, H. Wang, et al., Enhanced CO_2 photocatalytic reduction on alkali-decorated graphitic carbon nitride, *Appl. Catal. B* 216 (2017) 146–155.
- [6] L. Jiang, X. Yuan, Y. Pan, J. Liang, G. Zeng, Z. Wu, et al., Doping of graphitic carbon nitride for photocatalysis: a review, *Appl. Catal. B* 217 (2017) 388–406.
- [7] D. Wang, W. Gu, Y. Zhang, Y. Hu, T. Zhang, X. Tao, et al., Novel C-rich carbon nitride for room temperature NO_2 gas sensors, *RSC Adv.* 4 (35) (2014) 18003–18006.
- [8] J. Zhu, Y. Wei, W. Chen, Z. Zhao, A. Thomas, Graphitic carbon nitride as a metal-free catalyst for NO decomposition, *Chem. Commun.* 46 (37) (2010) 6965–6967.
- [9] T.Y. Ma, Y. Tang, S. Dai, S. Qiao, Proton-functionalized two-dimensional graphitic carbon nitride nanosheet: an excellent metal-/label-free biosensing platform, *Small* 10 (12) (2014) 2382–2389.
- [10] Q. Liang, Z. Huang, F. Kang, Q. Yang, Facile synthesis of crystalline polymeric carbon nitrides with an enhanced photocatalytic performance under visible light, *Chemcatchem* 7 (18) (2015) 2897–2902.
- [11] J. Liu, W. Li, L. Duan, X. Li, L. Ji, Z. Geng, et al., A graphene-like oxygenated carbon nitride material for improved cycle-life Lithium/Sulfur batteries, *Nano Lett.* 15 (8) (2015) 5137–5142.
- [12] J. Xiao, Y. Xie, F. Nawaz, Y. Wang, P. Du, H. Cao, Dramatic coupling of visible light with ozone on honeycomb-like porous $\text{g-C}_3\text{N}_4$, towards superior oxidation of water pollutants, *Appl. Catal. B* 183 (2016) 417–425.
- [13] Y. Cui, G. Zhang, Z. Lin, X. Wang, Condensed and low-defected graphitic carbon nitride with enhanced photocatalytic hydrogen evolution under visible light irradiation, *Appl. Catal. B* 181 (2016) 413–419.
- [14] X. Lin, D. Xu, R. Zhao, Y. Xi, L. Zhao, M. Song, et al., Highly efficient photocatalytic activity of $\text{g-C}_3\text{N}_4$ quantum dots (CNQDs)/Ag/ Bi_2MoO_6 nanoheterostructure under visible light, *Sep. Purif. Technol.* 178 (2017) 163–168.
- [15] X. Bai, L. Wang, R. Zong, R. Zhu, Photocatalytic activity enhanced via $\text{g-C}_3\text{N}_4$ nanoplates to nanorods, *J. Phys. Chem. C* 117 (19) (2013) 9952–9961.
- [16] Y. Wang, Y. Li, W. Ju, J. Wang, H. Yao, L. Zhang, et al., Molten salt synthesis of water-dispersible polymeric carbon nitride nanoseaweeds and their application as luminescent probes, *Carbon* 102 (2016) 477–486.
- [17] S. Wang, C. Li, T. Wang, P. Zhang, A. Li, J. Gong, Controllable synthesis of nanotube-type graphitic C_3N_4 and their visible-light photocatalytic and fluorescent properties, *J. Mater. Chem. A* 2 (9) (2014) 2885–2890.
- [18] P. Niu, L. Zhang, G. Liu, H.M. Cheng, Graphene-like carbon nitride nanosheets for improved photocatalytic activities, *Adv. Funct. Mater.* 22 (22) (2012) 4763–4770.
- [19] J. Tian, Q. Liu, C. Ge, Z. Xing, A.M. Asiri, A.O. Alyoubi, et al., Ultrathin graphitic carbon nitride nanosheets: a low-cost, green, and highly efficient electrocatalyst toward the reduction of hydrogen peroxide and its glucose biosensing application, *Nanoscale* 5 (19) (2013) 8921–8924.
- [20] H. Xu, J. Yan, X. She, L. Xu, J. Xia, Y. Xu, et al., Graphene-analogue carbon nitride: novel exfoliation synthesis and its application in photocatalysis and photoelectrochemical selective detection of trace amount of Cu^{2+} , *Nanoscale* 6 (3) (2014) 1406–1415.
- [21] F. Liang, L. Tian, H. Zhang, F. Liang, S. Liu, R. Cheng, et al., Low temperature synthesis of LiSi_2N_3 nanobelts via molten salt nitridation and their photoluminescence properties, *RSC Adv.* 6 (73) (2016) 68615–68618.
- [22] J. Liu, Z. Huang, C. Huo, F. Li, H. Zhang, S. Zhang, Low-temperature rapid synthesis of rod-like ZrB_2 powders by molten-salt and microwave Co-assisted carbothermal reduction, *J. Am. Ceram. Soc.* 99 (9) (2016) 2895–2898.
- [23] Z. Huang, H. Duan, J. Liu, et al., Preparation of lanthanum cerate powders via a simple molten salt route, *Ceram. Int.* 42 (8) (2016) 10482–10486.
- [24] Linfeng Ye, Feng Liang, Lei Zhao, et al., Facile synthesis of hexagonal boron nitride nanoplates via molten-salt-mediated magnesiothermic reduction, *Ceram. Int.* 41 (2015) 14941–14948.
- [25] M.J. Bojdys, J.O. Müller, M. Antonietti, A. Thomas, Ionothermal synthesis of crystalline: condensed, graphitic carbon nitride, *Chem. Eur. J.* 14 (27) (2008) 8177–8182.
- [26] E. Wirnhier, M. Döbinger, D. Gunzelmann, J. Senker, B.V. Lotsch, W. Schnick, Poly (triazine imide) with intercalation of lithium and chloride ions [$(\text{C}_3\text{N}_3)_2(\text{NH}_4\text{Li}_1)_2\text{Cl}$]: a crystalline 2D carbon nitride network, *Chem. Eur. J.* 17 (11) (2011) 3213–3221.
- [27] K. Schwinghammer, B. Tuffy, M.B. Mesch, E. Wirnhier, C. Martineau, F. Taullelle, et al., Triazine-based carbon nitrides for visible-light-driven hydrogen evolution, *Angew. Chem. Int. Ed.* 52 (2013) 2435–2439.
- [28] K. Schwinghammer, M.B. Mesch, V. Duppel, C. Ziegler, J. Senker, B.V. Lotsch, Crystalline carbon nitride nanosheets for improved visible-light hydrogen evolution, *J. Am. Chem. Soc.* 136 (5) (2014) 1730–1733.
- [29] M.B. Mesch, K. Bärwinkel, Y. Krysiak, C. Martineau, F. Taullelle, R.B. Neder, et al., Solving the hydrogen and lithium substructure of poly(triazine imide)/LiCl using NMR crystallography, *Chem. Eur. J.* 22 (47) (2016) 16878–16890.
- [30] W. Zheng, N.B. Wong, W. Wang, G. Zhou, A. Tian, Theoretical study of

- 1,3,4,6,7,9,9b-heptaazaphenalene and its ten derivatives, *J. Phys. Chem. A* 108 (2004) 97–106.
- [31] N. Tian, Y. Zhang, X. Li, K. Xiao, X. Du, F. Dong, et al., Precursor-reforming protocol to 3D mesoporous g-C₃N₄ established by ultrathin self-doped nanosheets for superior hydrogen evolution, *Nano Energy* 38 (2017) 72–81.
- [32] H. Gao, S. Yan, J. Wang, Y.A. Huang, P. Wang, Z. Li, et al., Towards efficient solar hydrogen production by intercalated carbon nitride photocatalyst, *Phys. Chem. Chem. Phys.* 15 (41) (2013) 18077–18084.
- [33] C. Pan, J. Xu, Y. Wang, D. Li, Y. Zhu, Dramatic activity of C₃N₄/BiPO₄ Photocatalyst with core/shell structure formed by self-assembly, *Adv. Funct. Mater.* 22 (7) (2012) 1518–1524.
- [34] R. Asahi, T. Morikawa, T. Ohwaki, K. Aoki, Y. Taga, Visible-light photocatalysis in nitrogen-doped titanium oxides, *Science* 293 (2001) 269–271.
- [35] C.P. Sajan, S. Wageh, A.A. Al-Ghamdi, J. Yu, S. Cao, TiO₂ nanosheets with exposed {001} facets for photocatalytic applications, *Nano Res.* 9 (1) (2016) 3–27.
- [36] X. Li, J. Yu, S. Wageh, A.A. Al-Ghamdi, J. Xie, Graphene in photocatalysis: a review, *Small* 12 (48) (2016) 6640–6696.
- [37] Y. Yao, B. He, F. Xu, X. Chen, Equilibrium and kinetic studies of methyl orange adsorption on multiwalled carbon nanotubes, *Chem. Eng. J.* 170 (1) (2011) 82–89.